ACS APPLIED

Development and Characterization of Transparent Hydrogen-Doped Indium Oxide Layers for Use in Selective Contacts of Germanium

Ermanno Sava,* Kai Gehrke, Stephan Heise,* Laura Campos Guzman, Martin Vehse, and Carsten Agert



Cite This: https://doi.org/10.1021/acsaem.5c02770

ENERGY MATERIALS

Thermophotovoltaic Cells



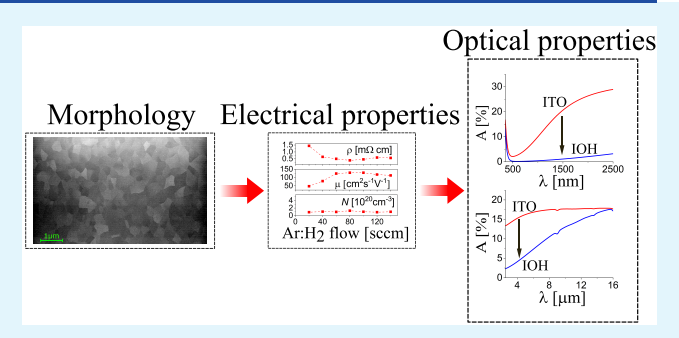
ACCESS

Metrics & More

Article Recommendations

s Supporting Information

ABSTRACT: Crystalline-germanium photovoltaic cells are promising candidates for thermophotovoltaics (TPV), but their potential is hindered by the difficulty in optimizing the out-of-band infrared reflectance of the back contacts. A proposed solution is to use reflective hole-selective back-contacts based on transition metal oxides (TMOs), contacted with indium tin oxide (ITO) and a silver mirror. We propose to substitute the ITO with a Hydrogendoped Indium Oxide (IOH) layer to improve the optical response of such contacts. To study the possibility of using IOH in TPV applications, we RF-sputter IOH films and characterize them morphologically, electrically and optically, with a focus on their



infrared (IR) optical properties, also including the complex refractive index of one IOH film from 350 nm to 16 μ m. We obtain films with resistivities as low as 0.39 m Ω ·cm and IR absorptions, from 2.5 to 16 μ m and weighted with a blackbody spectrum at 1200 °C, as low as 6.1%; by comparison the absorption of ITO was 15.9%. Furthermore, we perform optical simulations of germanium wafers with IOH or ITO, followed by a silver mirror, to show the potential gain in the reflected power. These results are made possible by the high carrier mobilities, up to 130 cm² V⁻¹ s⁻¹, that counterbalance the effect of low carrier concentrations on the electrical properties.

KEYWORDS: hydrogen-doped indium oxide, transparent conductive oxide, sputtering, thermophotovoltaics, germanium, selective contacts

INTRODUCTION

Thermophotovoltaics (TPV) is a concept for electricity generation in which the radiation power from a hot thermal emitter is converted to electrical power with proper photovoltaics (TPV) cells. TPV has been proposed for a range of applications, including heat-to-electricity energy conversion in thermal batteries, 2 direct solar energy conversion, 3 waste heat scavenging⁴ and space applications.⁵ The emitter is typically kept at a temperature between 1000 K and 2500 K, resulting in a spectrum peaked at higher wavelengths and more broadband than the solar spectrum used in standard photovoltaics. This results in a lower optimal bandgap and a high fraction of outof-band (OOB) photons. TPV has been first proposed in 1956,6 but has become attractive in the last years thanks to the development of highly reflective back-mirrors for the TPV cells, which enable the reflection of out-of-band photons back to the emitter. The realization of the importance of the back mirror resulted in a series of breakthroughs, 7,8 and recently a TPV power conversion efficiency η_{TPV} = 44.0% with a single junction cell has been shown.9 The best TPV cells up to date are based on InGaAs, but alternative materials are desirable for the development of potentially cheaper TPV cells.

A promising material for TPV cells is crystalline germanium (c-Ge), because of its ideal bandgap of 0.66 eV, its lower price, as compared to InGaAs, and because there is already established market for big sized Ge wafers. 10 Different architectures for Ge TPV cells have been proposed, 10-14 with the most recent record TPV power conversion efficiency being $\eta_{\rm TPV} = 23.2\%.^{14}$ In 2023 Martin et al. proposed to use back hole selective contacts (HSCs) consisting of transition metal oxides (TMOs) in contact with Au or an ITO/Ag stack. They obtain their best out-of-band reflectance R_{OOB} = 87.5% with a MoOx/ITO/Ag stack. The reflectance was limited by the free carrier absorption (FCA) of their ITO layer, which is needed in HSCs as a barrier against Ag diffusion and furthermore improves hole transport thanks to its high work function. 16 A possible route to improve R_{OOB} is to optimize the ITO deposition process. Alternatively, one could substitute ITO with another transparent conductive oxide (TCO), such as hydrogen-doped indium oxide (IOH), which has a much

September 3, 2025 Received: Revised: October 22, 2025 Accepted: November 10, 2025



ACS Applied Energy Materials

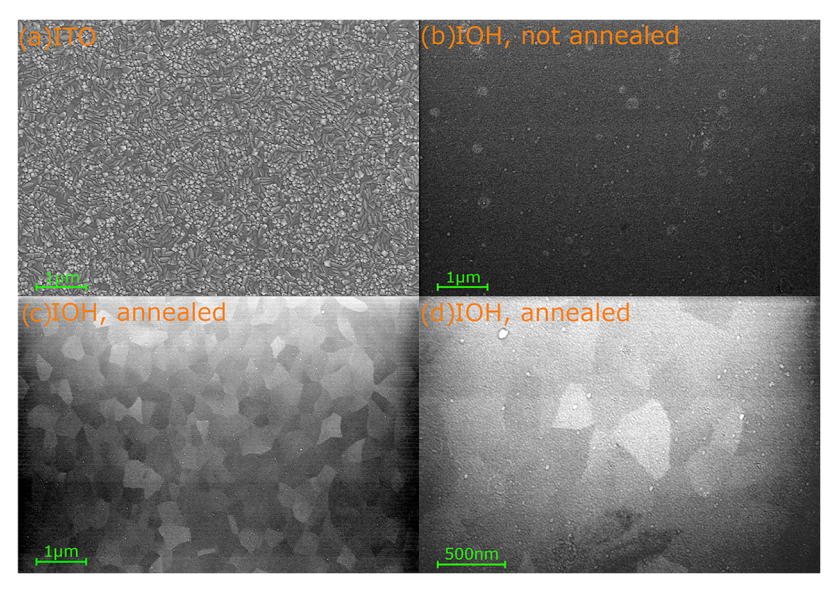


Figure 1. SEM scans of TCO samples. (a) ITO reference sample, the magnification is 40k× (b) not annealed IOH sample, the magnification is 40k× (c, d) annealed IOH sample, the magnification is 15k×: the grain structure of IOH is visible (d) same annealed IOH sample as (c), the magnification is 40k×: a nanocrystalline substructure is also visible. The IOH samples were deposited using 20 sccm Ar/O₂ and 80 sccm Ar/O₃.

lower FCA and similar resistivity thanks to its lower carrier concentration and higher carrier mobility. ^{17–19} Here we show the feasibility of using IOH for the back contact of Ge TPV cells. Magnetron sputtered IOH layers are characterized electrically and optically up to the mid-infrared (MIR), which at the best of our knowledge has never been done. We compare the results to that of reference ITO layers. The results are also useful for other applications of TCOs.

EXPERIMENTAL SECTION

The substrates used for the depositions of the IOH and the reference ITO films were 1 mm thick glass microscope slides and 300 μ m-thick crystalline Si wafers provided by Soka. The microscope slides were used for the electrical characterization of the films, SEM, profilometry and for optical spectroscopy (UV–vis-NIR) measurements. The Si wafers were float-zone (FZ) grown and low-doped, with nominal resistivities $\rho > 1k\Omega \cdot \text{cm}$. Single side polished (SSP) wafers were used for spectroscopic ellipsometry (SE), while double side polished (DSP) wafers were used for Fourier-transform infrared (FTIR) spectroscopic measurements.

A Singulus Vistaris 600 in-line magnetron sputter coater was used for depositing 100 nm thick TCO layers. Direct current (DC) sputtering was used for the ITO depositions. The power applied to the ITO target was 2000 W (3.33 W·cm⁻²), and the gas fluxes were 500 sccm Ar and 9 sccm O2, corresponding to a process pressure of 9.96·10⁻³ mbar. In addition, the carrier was heated to 260 °C. For depositing IOH layers, radio frequency (RF) sputtering was used with an indium oxide (In_2O_3) target in an atmosphere including Ar, O_2 , and H₂. The oxygen was provided by a 95:5% Ar/O₂ gas mixture and the hydrogen by a 98:2% Ar/H₂ gas mixture. The applied power was 900 W (1.50 W·cm⁻²); this power was chosen having in mind a low damage deposition for future integration of the IOH with MoO_x. The Ar/O₂ gas flux was varied from 0 to 30 sccm (implying an O₂ content from 0% and 0.5%), and the hydrogen flow was varied from 0 to 140 sccm Ar/H₂ (corresponding to a H₂ content from 0% and 0.93%). During the depositions, the total gas flow was fixed to 300 sccm, resulting in the total pressure being ca. $3.30 \cdot 10^{-3}$ mbar. The layers were deposited with no intentional heating. After the depositions, the IOH samples were annealed in air at 200 °C for 30 min. Other annealing conditions have been tried, whose results were less ideal (see Supporting Information).

The thicknesses of the samples were measured with a profilometer (DektakXT by Bruker). A SEM microscope (Gemini by Zeiss) was used to observe their morphology and qualitatively confirm the annealing induced recrystallization for IOH layers. The sheet resistance was measured with a 4-point-probe (4PP) device (RM3-AR by Jandel). The carrier mobility μ and the carrier concentration N were measured with a Hall effect measurement setup (HL5500 by Nanometrics), using the Van der Pauw (VdP) method. The device has a permanent magnet with a magnetic field B=0.5 T. During the measurements the current was fixed at I=0.1 mA. For preparing VdP measurements, samples deposited on glass were cut into squares and triangular VdP contacts were subsequently deposited at the edge of the squares by sputtering Ag through a shadow mask.

The optical characterization was carried out in the wavelength range from 350 nm to 16 μ m. All samples have been characterized from 350 to 2500 nm in transmittance (T) and reflectance (R) measurements with a UV—vis-NIR spectrometer using a diffuse reflectance integration sphere (Cary-Series UV—vis-NIR and DRA-2500 by Agilent Technologies). Near-infrared (NIR) and mid-infrared (MIR) R and T measurements in the wavelength range from 2.5 to 16 μ m have been taken with a FTIR spectrometer (PerkinElmer Frontier) and a gold integrating sphere (Mid-IR IntegratIR by Pike Technologies). For R measurements the angle of incidence was 12°. Moreover, Ellipsometry measurements have been carried out in the wavelength range from 350 to 1700 nm at 50°, 60°, and 70° with an UV—vis-NIR ellipsometer (Woollam RC2-DI).

The optical data has been analyzed with the software CODE, 20 by fitting appropriate optical models with the experimental data. The model used to describe the sample comprises 2 layers: the substrate (glass or silicon) and the thin films (ITO or IOH); the optical response is computed with the transfer matrix method, considering the angle of incidence and the polarization. From the analysis the light absorption of the films could be extracted, together with the $n\kappa$ data, where ellipsometry measurements were available. This procedure was chosen to compensate for the absorption of the substrates, which was expected to be non-negligible especially for the FTIR measurements. Furthermore, CODE has been used to simulate the reflectance of a Ge wafer with a back stack consisting of an IOH or ITO thin film, followed by an Ag back mirror.

In order to identify the IOH layers with the best electrical properties, 4PP and Hall measurements were taken by iteratively varying O_2 and H_2 . In the first phase of the optimization, 4PP measurements were used to find a range of O_2 and H_2 content in which the resistance was sufficiently low. For instance, samples with

ACS Applied Energy Materials

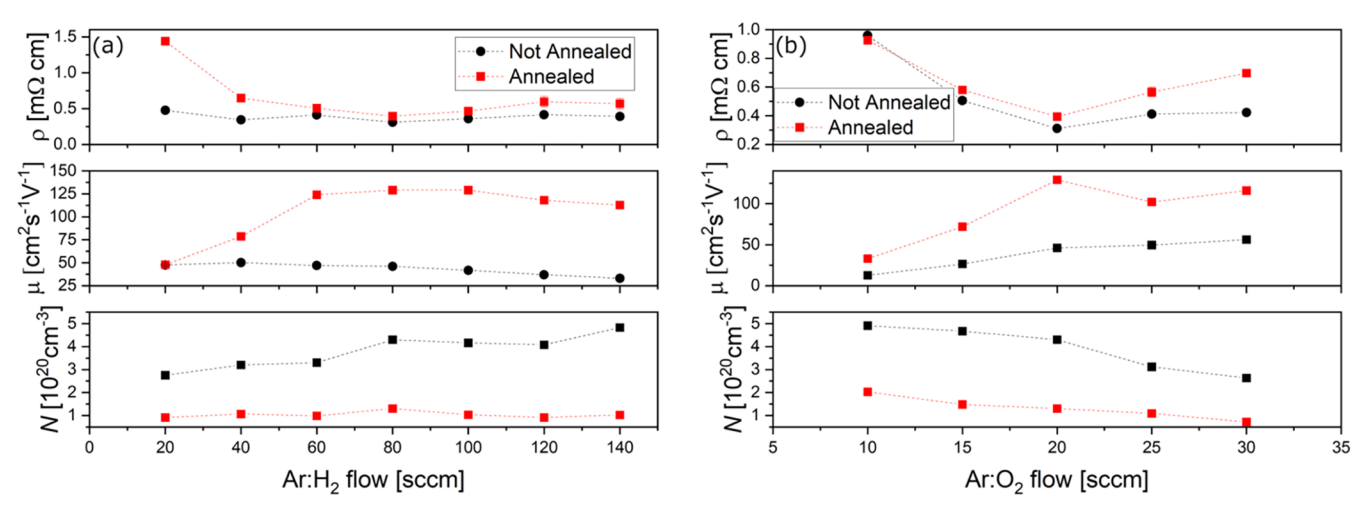


Figure 2. Results of the electrical characterization of IOH films deposited at different conditions, before and after annealing: (a) varying Ar/H_2 content, with 20 sccm Ar/O_2 and (b) varying the Ar/O_2 content, with 80 sccm Ar/H_2 .

varying O_2 content for a given H_2 content were analyzed, and the O_2 that minimized the sheet resistance was taken for the next step, in which the optimal H_2 content was located. After this phase, in addition to 4PP measurements, Hall measurements have been taken, and a similar iteration has been repeated, looking for the maximum carrier mobility and lowest resistivity. During this phase, UV-vis-NIR R and T measurements have been carried out in parallel.

The recipes that gave the highest mobilities and lowest resistivities have been used to deposit further samples to be characterized with the FTIR and the best sample has been characterized with the ellipsometry. In addition, the ITO sample has been fully characterized electrically and optically for comparison. The deposition parameters of all prepared samples can be found in Tables S1–S3 in the Supporting Information.

■ RESULTS AND DISCUSSION

SEM images were taken for both ITO and IOH films to investigate their microstructure. IOH films have been measured before and after annealing to check whether the annealing recrystallizes the films. The results are shown in Figure 1: The as-deposited ITO and IOH samples are shown in (a) and (b), while (c) and (d) show the results for annealed IOH films at 15k× and 40k× magnification. It can be seen that there is a drastic change of morphology: before annealing, the IOH samples are more uniform, with a visibly granular structure. On the other hand, annealed samples are characterized by grains with sizes between 200 and 500 μ m, which are visible in Figure 1c,d. An additional substructure is also visible (see Figure 1d). It must be noted that SEM images taken with EBS detectors bear information about the surface and that alone they do not prove the full recrystallization of the IOH films. Nevertheless, the recrystallization of IOH has been already proved by means of XRD and EBSD, ^{19,21} and the grain structure observed with the SEM is consistent with these EBSD images. Therefore, the observation of grains with the SEM scans provides a relatively quick way to qualitatively confirm the recrystallization of the films.

In order to understand the differences between the electrical and optical properties of IOH and ITO, one has to consider the carrier mobility μ and the carrier concentration N. On the one hand, the resistivity is related to both N and μ by the equation $\rho^{-1} = e\mu N$. On the other hand, the IR optical behavior of the films is characterized by the intraband transitions of the free carriers, and is well described by the

Drude model (see Supporting Information). According to this model N is related to the plasma carrier frequency by $\omega_P = \sqrt{\frac{Ne^2}{\varepsilon_0 \varepsilon_\infty m^*}}$, where ε_0 is the vacuum permittivity, ε_∞ is the high-frequency permittivity of the material, and m^* is the

high-frequency permittivity of the material, and m^* is the effective mass of the carriers (electrons for ITO and IOH). The resulting free carrier absorption (FCA) increases with the wavelength. Moreover, a lower plasma frequency results in a lower absorption in the IR band. Hence, a trade-off between a low resistance and a low IR absorption is given. In addition, it should be mentioned that from a microscopic point of view both μ (and therefore ρ^{-1}) and ω_P depend on the carrier concentration N, the effective mass m^* and on the relaxation time τ . Importantly, τ depends on grain-boundary scattering, which is much lower in IOH thanks to its relatively big grains. The same permittivity of the same permitted in the same permittivity of the same permitted permittivity of the same permitted permitte

The results of the electrical characterization of IOH samples with varying O2 and H2 content near the optimum value of the highest mobility and the lowest resistivity are shown in Figure 2. The top part of the graphs shows the resistivity, computed as $\rho = R_S \cdot t$, where R_S is the sheet resistivity and t is the thickness. The middle part of the graphs shows the Hall mobility μ and the bottom part shows the bulk carrier concentration N. Regarding the O2 optimization, it can be seen that the resistivity has a minimum for the flow $Ar/O_2 = 20$ sccm, and that both lower and higher O₂ contents result in a lower carrier mobility and higher resistivity. A similar behavior is observed for a varying H2 content, with a minimum of the sheet resistivity at Ar/H₂ = 80 sccm. Nevertheless, the resistivity remains low even for high Ar/H2 flows. In addition, it can be seen that the resistivity is more sensible to O₂ flux changes during the deposition. This behavior was always observed during the optimization iterations. Regarding the Hall measurements, one can see that annealing always results in a decrease of the carrier concentration, and that increasing O2 content results in a lower carrier concentration. This is expected because a greater O2 content in the films results in less O2 vacancies and therefore less free electrons, and it explains the high resistivities observed for Ar/O2 flows greater than 20 sccm. On the other hand, the carrier concentration before annealing increases with the H2 content, while its value after annealing seems independent of the H2 content. Regarding the behavior of μ , by changing the O₂ content

Table 1. Results of the Electrical Characterization of the TCO Films Deposited for Both Electrical and Complete Optical Characterization from 300 nm to 16 μ m

sample	Ar/O_2 [sccm]	Ar/H ₂ [sccm]	thickness [nm]	$ ho \; [\mathrm{m}\Omega{\cdot}\mathrm{cm}]$	$\mu \ [\mathrm{cm^2 \ V^{-1} \ s^{-1}}]$	$N [10^{20} \text{ cm}^{-3}]$
ITO	n.a.	n.a.	97 ± 5	0.30 ± 0.02	36.7 ± 0.7	6.2 ± 0.3
IOH 216	20	80	99 ± 2	0.61 ± 0.01	127 ± 1	0.8 ± 0.2
IOH 199	20	60	102 ± 3	0.36 ± 0.01	134 ± 2	1.32 ± 0.04
IOH 200	20	100	102 ± 2	0.54 ± 0.01	97 ± 1	0.87 ± 0.02

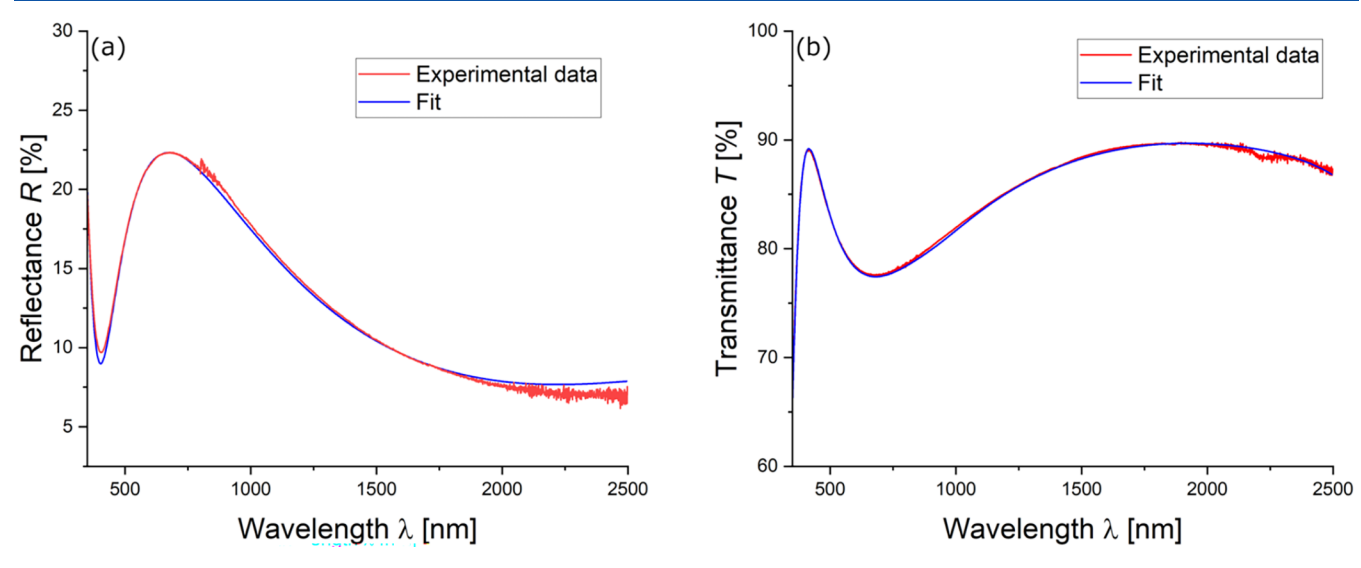


Figure 3. (a) Reflectance and (b) transmittance measurements and their fits for an annealed IOH sample (IOH 212, see Supporting Information), deposited with 20 sccm Ar/ O_2 and 80 sccm Ar/ H_2 .

one can see a maximum at $Ar/O_2=20$ sccm, where also the minimum resistivity is observed. By changing the Ar/H_2 , two regimes can be seen: fluxes below 60 sccm result in lower mobilities which increase with the flux, whereas higher fluxes result in very high mobilities above 130 cm² V⁻¹ s⁻¹. The highest mobilities have been observed for oxygen flux $Ar/O_2=20$ sccm and Ar/H_2 fluxes between 60 and 100 sccm, with mobilities up to $\mu=130$ cm² V⁻¹ s⁻¹, comparable to state-of-the-art IOH.

Table 1 resumes the electrical properties of the reference ITO layer and IOH layers which have been deposited with the optimal recipes for subsequent analysis. The ITO has the lowest sheet resistance thanks to its high carrier concentration and in spite of its relatively low mobility. Nevertheless, the high carrier concentration is also expected to (and indeed does) increase the FCA of the layer, degrading the optical properties and limiting the IR reflectance of back selective contacts in both PV cells. To the other side, annealed IOH has a lower carrier concentration whose influence on the resistivity is compensated by its high mobility, resulting in a similarly low resistivity as for ITO.

All samples investigated with the Hall setup during the optimization have been also analyzed in the UV—vis-NIR band with UV—vis-NIR spectroscopy, taking R and T spectra and fitting both curves with an optical model. More details about the optical model can be found in the Supporting Information. Figure 3 shows the experimentally observed reflectance on the left and transmittance on the right side for an annealed IOH layer and its related fit.

The optical model was used to fit the data and calculate the single layer absorption of the TCO in the wavelength range from 350 to 2500 nm. Figure 4 compares the absorption of

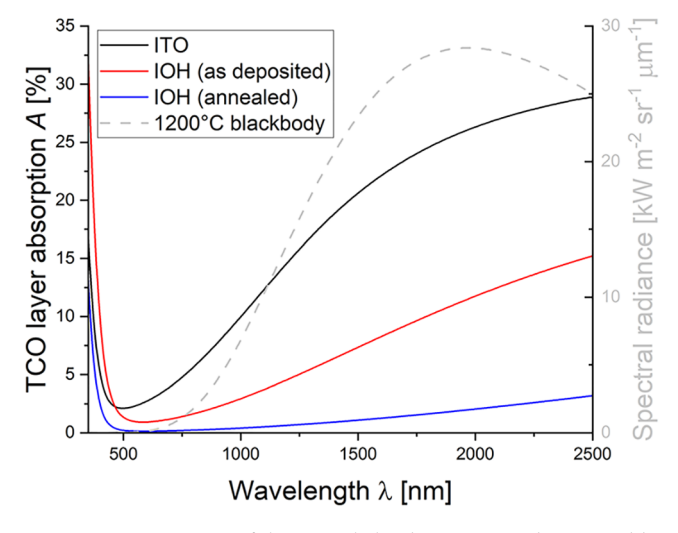


Figure 4. Comparison of the TCO light absorption as determined by the fit procedure for ITO sample and IOH 212, the latter being deposited with 20 sccm Ar/O_2 and 80 sccm Ar/H_2 . The spectrum of a blackbody at 1200 °C is also shown for reference.

ITO and IOH layers (before and after annealing). It can be seen that all TCOs have a low absorption in the visible range, and that ITO is the most absorptive, reaching 4.8% absorption at 750 nm, at the edge of the visible spectrum. The absorption of TCOs increases with the wavelength and for ITO it almost reaches 29% at 2500 nm. By comparison, IOH absorbs less visible and IR light both before and after annealing. Before annealing the IOH layer absorption is 1.4% at 750 nm and 15% at 2500 nm. Nevertheless, annealing drastically reduces the absorption to 0.2% at 750 nm and 3.0% at 2500 nm. These

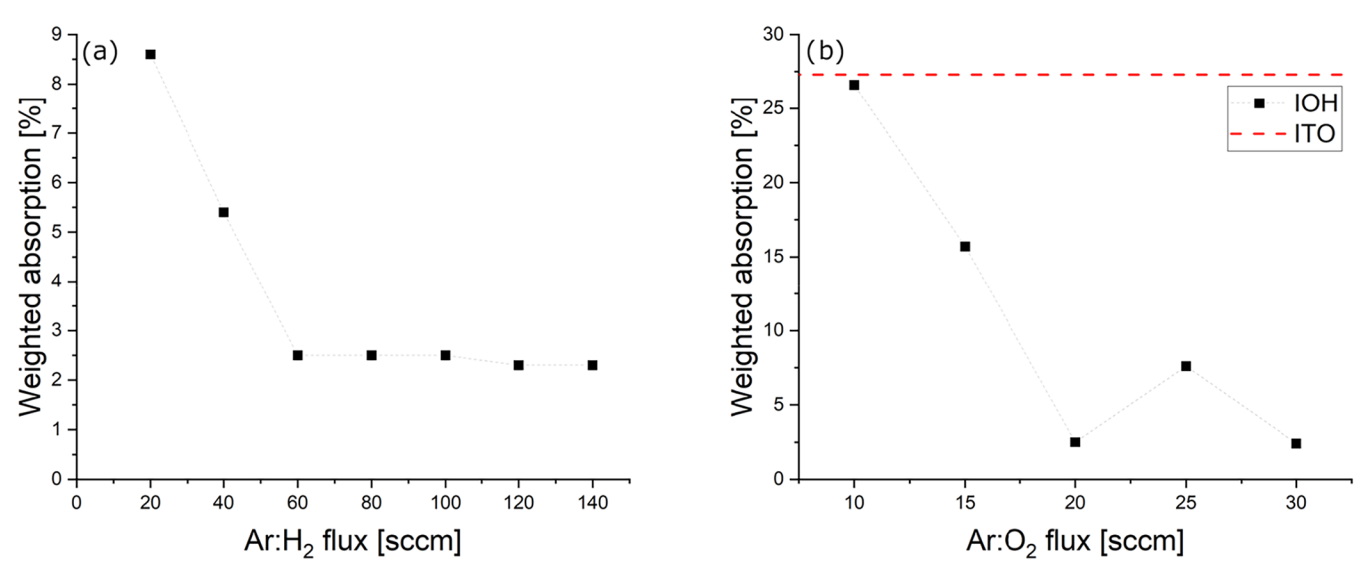


Figure 5. Absorption of the IOH film deposited at different conditions, weighted with a blackbody spectrum at 1200 $^{\circ}$ C: (a) films deposited with varying H₂ content and (b) films deposited with varying O₂ content, a red line corresponding to the weighted absorption of ITO has also been added for reference.

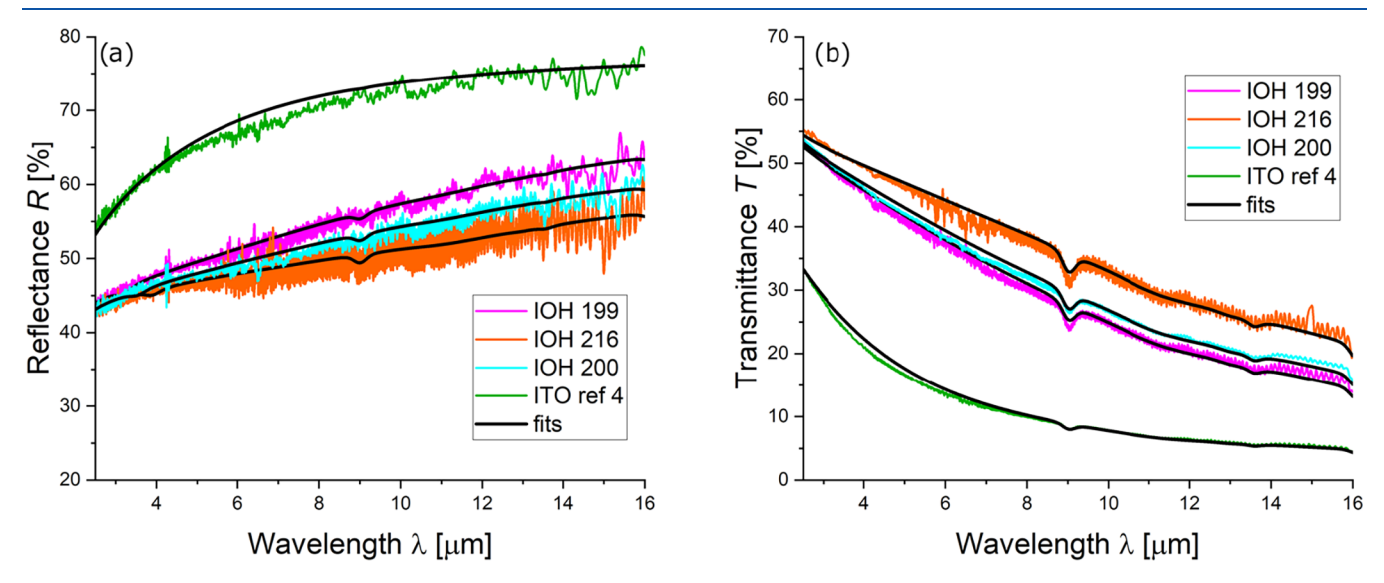


Figure 6. Transmittance (a) and reflectance (b) FTIR spectra of the IOH samples and of ITO, together with their fits. Note that lower carrier concentrations result in higher transmittances and lower reflectances.

facts are explained by the effect of *N* on the FCA in the films and show one of the main advantages of IOH over ITO in applications where visible or IR absorption is a matter of concern, such as in TPV.

For a first quantification of the quality of the IOH layers for TPV applications, the weighted absorption of the layers with a blackbody at 1200 $^{\circ}$ C has been computed in the band between 1880 nm (corresponding to the bandgap of Ge, i.e., 0.66 eV)

and 2500 nm as
$$A_{\rm W}=rac{\int_{E_{
m min}}^{E_{
m max}}A(E)\cdot\phi(E)\cdot{
m d}E}{\int_{E_{
m min}}^{E_{
m max}}\phi(E)\cdot{
m d}E}$$
, where $E=hc/\lambda$ is the

energy of the photons, E_{\min} and E_{\max} are respectively the minimum and maximum energies in the relevant band, A(E) is

the layer absorption and
$$\phi(E) = \frac{2\pi}{h^3c^2} \cdot E^2 \cdot \left(\exp\left(\frac{E}{k_{\rm B}T}\right) - 1 \right)^{-1}$$
 is

the photon flux of a blackbody at temperature T, assuming a solid angle equal to π sr.²⁶ The Results are shown in Figure 5. The weighted absorption of the ITO layer is 27.3%, while

annealed IOH films have consistently lower absorption, the lowest being 2% and found for the IOH film deposited with 20 sccm ${\rm Ar/O_2}$ and 80 sccm ${\rm Ar/H_2}$. Nevertheless, for ${\rm Ar/H_2}$ fluxes greater than 60 sccm the weighted absorption is always around 2.5%, without showing a clear minimum. Therefore, the samples with the greatest μ and lowest sheet resistance are found to be also the ones with the lowest NIR absorption.

In a next step, the samples described in Table 1 have been analyzed optically in the UV–vis-NIR and in the NIR-MIR range. All these samples have been characterized with the UV–vis-NIR and the FTIR. In addition, the sample IOH 216 has also been characterized with ellipsometry. Figure 6 shows the FTIR data from 2.5 μ m to 16 μ m of all the samples and their fit with a Drude model.

The FTIR fits have been used to compute the IR absorption A of the TCO layers from 2.5 μ m to 16 μ m, as shown in Figure 7. Note that the absorption at 2.5 μ m with the FTIR is in general different than the one obtained at 2.5 μ m with the

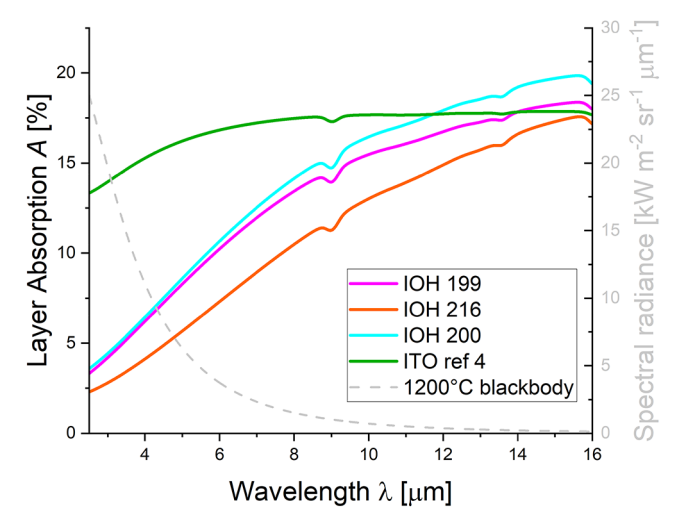


Figure 7. Comparison of the infrared (IR) TCO light absorption as determined by the fit with the Drude model for the IOH samples and the ITO reference. The spectrum of a blackbody at 1200 $^{\circ}$ C is also shown for reference. The IR absorption is due to free carrier absorption (FCA) and its increase with the wavelength is related to the plasma frequency. Note that despite its higher carrier concentration, the sample IOH 199 absorbs less IR light than IOH 200.

UV-vis-NIR: this is because of the different refractive indices of the substrates used for the experiments, which are also responsible for the different transmittance and reflectance.

As expected, the sample IOH 216 has the lowest absorption, thanks to its low carrier concentration. Nevertheless, the sample IOH 199 has a lower IR absorption than IOH 200, in spite of the higher carrier concentration; this can be explained by the higher reflectance of the former, which compensates for the lower transmittance. The absorption of all IOH samples increases visibly with the wavelength throughout the range in consideration. On the other hand, ITO has the highest carrier concentration and therefore the highest plasma frequency, which results in a much higher FCA for the shorter IR wavelength. Nevertheless, the high plasma frequency results in a very low increase of the absorption with the wavelength, so that some of the IOH samples become more absorptive for wavelengths greater than 10 μ m. Note that the region where the IOH is more absorptive is far from the peak of emission of the thermal emitters used in TPV, as it can be seen by looking at the blackbody radiance spectrum; therefore, the contribution to the weighted absorption is very low.

The results for the IR absorption have been used to compute the weighted absorption of the TCO in the same range. Moreover, the absorption data in the visible and in the IR range have been combined to estimate the weighted absorption between 1.88 μ m and 16 μ m. Nevertheless, one has to keep in

mind that the substrates are different for UV—vis-NIR data and the FTIR data, and that the target application requires germanium substrates. Therefore, these results are to be taken only qualitatively. Table 2 shows the results of the analysis for the weighted absorption.

Finally, the spectroscopic ellipsometry data and the UV–vis-NIR data have been used to determine more accurately the complex refractive index of the IOH 216 sample in the range between 350 and 2500 nm, and the FTIR fit with the Drude model has been used to estimate the complex refractive index of the same sample, from 2.5 μ m to 16 μ m. The results are shown in Figure 8. The ellipsometry data is provided in Figure S3 in the Supporting Information.

When comparing these results with the results of other studies, it must be noted than besides the characteristics of the deposition machines, there are many parameters which can be optimized: for instance, IOH films can be deposited with both pulsed DC and RF sputtering, using either H₂O or a mixture of H₂ and O₂, with different pressures etc. Moreover, different annealing environments, temperatures and durations can be studied. As an example, Schuldes et al. optimized IOH films in similar conditions, using RF sputtering with Ar/H₂ and Ar/O₂ mixtures and annealing in air at 200 °C for 30 min, but a higher pressure. 18 They obtained mobilities up to 90 cm² V⁻¹ s⁻¹ and higher carrier concentrations around $2 \cdot 10^{20}$ cm⁻³, which in turn result in resistivities around 0.4 m Ω ·cm, and in spite of the relatively high value of N they report a low 1.28% IR absorption from 800 to 1300 nm, weighted with the AM 1.5G spectrum. By comparison, the IOH films presented in this work have higher carrier mobilities, which enable similar resistivities with lower carrier concentrations.

The IOH process has been developed for subsequent use in optoelectronics devices, in particular TPV cells. Most TPV cells are designed to minimize the IR OOB parasitic absorption, because reflected OOB photons can be reabsorbed by the thermal emitter, avoiding excessive heating of the cells and at the same time increasing the overall efficiency. In order to accomplish these goals many device architectures have been developed, including air-bridges, dielectric layers²⁷ etc. The IOH layers shown in this study target a specific device architecture proposed by Martin et al.,15 which employs Ge as the active material and reflective back hole-selective contacts, consisting of 1D stacks of a transition metal oxide TMO and a metal mirror. One of the problems of this architecture is that silver mirrors contacted with ITO to the TMO layers are more reflective but also have worse electrical properties than gold mirrors in direct contact with the TMO. In particular, the best reflectance is 87.5% observed with a MoO_x/ITO/Ag stack. The FCA of ITO limits the reflectance of the contact and therefore of the TPV cell. In spite of the limitation of the absorption analysis, which has been carried out on glass and

Table 2. Weighted Absorption at Different Ranges for the ITO Reference and the IOH Samples^a

sample	Ar/O ₂ [sccm]	$\begin{array}{c} Ar/H_2 \\ [sccm] \end{array}$	NIR weighted absorption (1880–2500 nm) [%]	IR weighted absorption (2.5–16 μ m) [%]	weighted absorption (1.88–16 μ m) [%]
ITO	n.a.	n.a.	27.3	15.9	17.5
IOH 216	20	80	0.8	6.1	5.4
IOH 199	20	60	3.0	8.2	7.5
IOH 200	20	100	3.5	8.6	7.9

[&]quot;The investigated ranges are the NIR range from 1880 nm (i.e., the bandgap of Ge) to 2500 nm, using UV-VIS-NIR data (left); the IR range from 2.5 μ m to 16 μ m (center), using FTIR data; and the range from 1.88 μ m to 16 μ m, using all the data (right).

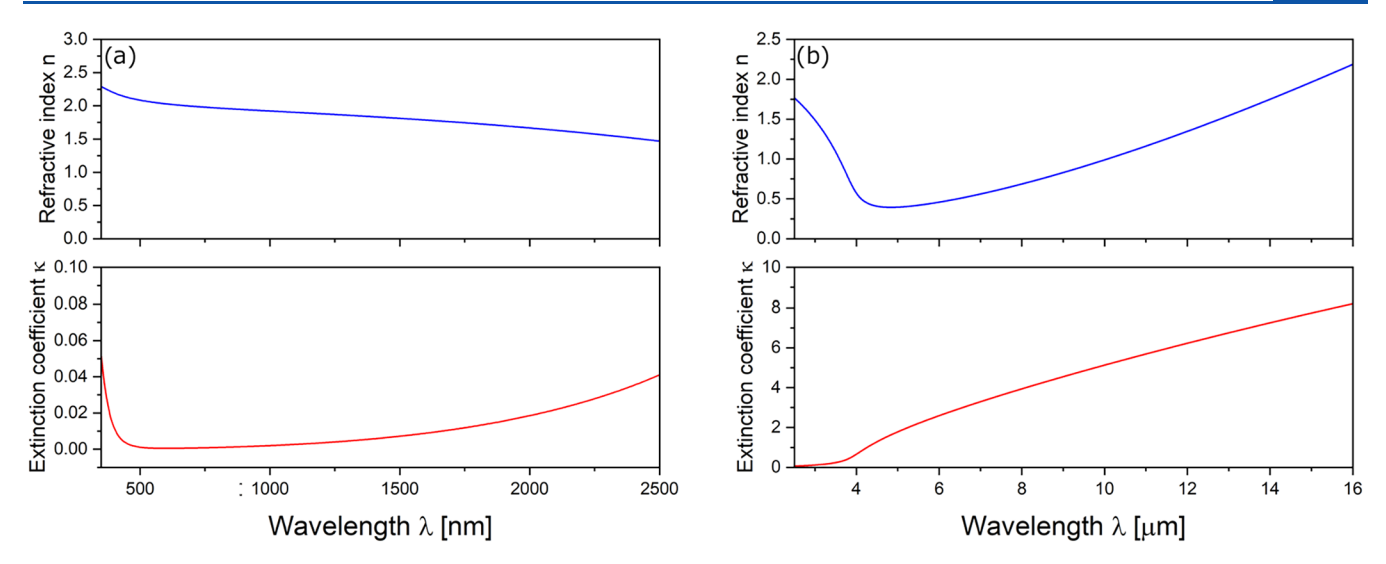


Figure 8. Complex refractive index extracted for the sample IOH 216. (a) In the range from 350 to 2500 nm with the use of UV-vis-NIR spectrometry and spectroscopic ellipsometry. (b) In the range from 2.5 to 16 μ m with the use of FTIR.

silicon, the low IOH weighed absorption shows the potential to increase sensibly the performance of the selective contact taken into consideration. In addition, one must consider that the IOH layers shown here are much thicker than the ones considered by Martin et al. (ca. 20 nm), which means that if thin recrystallized IOH layers could be obtained in contact with MoO_x and Ag, then the absorption contribution of the TCO would be even further suppressed. Nevertheless, it must be noted that the integration of IOH with the other materials is challenging, because of the possible sputtering damage of IOH on MoO_x and because of the sensibility of MoO_x with annealing.

Nevertheless, in order to provide a preliminary assessment of the performance of the contacts, the OOB reflectance of the contacts has been computed with CODE. A simplified layer stack has been assumed, consisting of a 175 um thick Germanium wafer in contact with 100 nm of IOH or ITO, followed by Ag. The refractive index and absorption coefficient published by Blanco et al. for intrinsic germanium wafer have been used to model the wafer.²⁸ The reason for using intrinsic germanium is to estimate an upper bound of the reflectance. IOH and ITO are modeled with the complex refractive indices obtained in this work (for ITO without ellipsometry). The complex refractive index of Ag was taken by the database of CODE. MoOx films have not been included because, at the best of the knowledge of the authors, complex refractive indices of MoOx are not yet available in the IR. The soobtained reflectance has been then used to estimate the OOB power reflected back to the emitter in a TPV system, using P_{ref} = $\int_{\lambda_{\text{Bandrap}}}^{\lambda_{\text{MAX}}} R(\lambda) \cdot B(\lambda) d\lambda$, where P_{ref} is the reflected power density, $\lambda_{\mathrm{Bandgap}}$ = 1880 nm corresponds to the bandgap of Ge, λ_{MAX} = 16 μ m, $R(\lambda)$ is the reflectance of the contact and $B(\lambda) = VF \cdot 2\pi hc^2 \cdot \lambda^{-5} \cdot \left(\exp\left(\frac{hc}{\lambda k_B T}\right) - 1\right)^{-5}$ is the blackbody spectral irradiance, which depends on the view factor VF. Table 3 shows, for different values of VF, the incoming power density $P_{\rm inc} = \int_{\lambda_{\rm Bandgap}}^{\lambda_{\rm MAX}} B(\lambda) d\lambda$ hitting the TPV cells and the reflected power density $P_{\rm ref}$. In addition, for both contacts the average OOB reflectance R_{OOB} of the contacts is also shown in brackets.

Table 3. Simulated Incoming Power $P_{\rm inc}$ and Reflected Out-of-Band Power $P_{\rm ref}$ of the Ge/TCO/Ag Stacks, Where the Ge Substrate is Considered to be Intrinsic and the TCO is Either IOH or ITO^a

		P _{ref} [W	√·cm ⁻²]
VF	$P_{\rm inc} [W \cdot {\rm cm}^{-2}]$	IOH ($R_{OOB} = 91.1\%$)	ITO $(R_{OOB} = 85.6\%)$
0.15	3.97	2.62	2.47
0.5	13.22	8.72	8.24
0.7	18.51	12.21	11.53
1.0	26.45	17.44	16.47

 $^{\prime\prime}P_{\rm inc}$ and $P_{\rm ref}$ are computed assuming a blackbody emitter at 1473 K and different view factors VF. The average OOB reflectance is also shown in brackets for each stack.

Naturally, the stacks employing IOH perform better than those with ITO. For comparison, Martin et al. reported a contact with a 20 nm thick ITO film, for which R_{OOB} = 87.5%; they also estimate $P_{\text{ref}} = 2.67 \text{ W} \cdot \text{cm}^{-2}$ for VF = 0.15. Note that they used a 1.2 Ω ·cm germanium wafer and that they integrate from 0.2 eV (i.e., λ_{MAX} = 6.2 μ m) to the bandgap of germanium. The TPV efficiency is defined as $\eta_{\text{TPV}} = P_{\text{out}}/P_{\text{abs}} =$ $P_{\text{out}}/(P_{\text{inc}} - P_{\text{ref}})$, where P_{out} is the output power and $P_{\text{abs}} = P_{\text{inc}}$ - $P_{\rm ref}$ is the power absorbed in the TPV cell. If one considers two TPV cells with the same P_{out} and respectively employing the IOH and the ITO contact, it follows that the former has a TPV efficiency ca. 10% higher than the latter (note that this does not depend on VF as both $P_{\rm inc}$ and $P_{\rm ref}$ are proportional to the view factor). Nevertheless, it must be noted that the doping of Ge results in FCA which impacts both R_{OOB} and P_{ref} Furthermore, while lower doping results in better reflectance, it also implies a higher resistivity, which is a serious issue for TPV devices, as they are expected to operate with currents of the order of 1 to 10 A·cm⁻², where resistive effects are important and result in a significant degradation of the fill factor.

Another important factor impacting the TPV efficiency is the contact resistivity of the HSCs. At the best of the knowledge of the authors, contacts using IOH have been mainly researched for the front contact of silicon solar cells or for thin film solar cells, ^{29–31} which are not comparable to the present case. In addition, both the contact resistivity and the passivation of the contacts depend on many parameters, such

as the deposition technique and its conditions, the doping of the substrate, the presence of a back surface field etc. Therefore, further work is needed to determine the electrical performance of the contacts and their potential use in TPV applications. Nevertheless, the contact resistivity and surface recombination velocity of the MoO_x/ITO/Ag contact shown by Martin et al. are still far from optimal. A more complete analysis of the electrical performance of the contacts, the effect of the introduction of MoO_x, the effect of different low doping concentrations of Ge on the optical and electrical properties and of TPV cells using the final contacts, and of the possibility of finding a suitable trade-off between these properties, are beyond the scope of the paper.

CONCLUSIONS

In this study the optimization of IOH thin films and the electrical and optical characterization of the optimized films has been shown. Furthermore, the IOH films have been compared to a reference ITO film. In particular, the films have been characterized in the NIR-MIR range up to 16 μ m, having in mind applications of the films in TPV cells. In addition, some preliminary optical simulations have been performed to assess the potential of the MoO_x/ITO/Ag hole selective contacts. The results confirm indeed that IOH has advantageous optical properties compared to ITO while maintaining good electrical properties, thanks to its higher carrier mobility and lower carrier concentration. Nevertheless, ITO still has a slightly lower sheet resistance. Moreover, there are other phenomena that should be taken into consideration, when choosing the TCO to be used as the contact material between the carrier selective material (here for instance MoO_x) and the silver back mirror and contact: for instance, the contact resistivity between the layers of the stack has to be determined, or the effect of possible chemical reactions at the interfaces must be assessed. Therefore, it is still unknown whether using IOH instead of ITO in the stack proposed by Martin et al. 1 will result in a better back cell and more work is needed to develop and characterize the stack. However, beside the field of TPV, the results of this work will be beneficial other applications where materials with high conductivity and low IR absorption are needed, for instance in solar cells and transparent electrodes for IR photodetectors and IR LEDs.²⁴

ASSOCIATED CONTENT

Supporting Information

The Supporting Information is available free of charge at https://pubs.acs.org/doi/10.1021/acsaem.5c02770.

Considerations on gas pressure, wobbling and RGA, effect of the annealing temperature, details of the optical models, results of the fits, ellipsometry and UV-vis-NIR data (PDF)

AUTHOR INFORMATION

Corresponding Authors

Ermanno Sava — German Aerospace Center (DLR), Institute of Networked Energy Systems, 26129 Oldenburg, Germany; orcid.org/0009-0005-2699-6488;

Email: ermanno.sava@dlr.de

Stephan Heise – German Aerospace Center (DLR), Institute of Solar Research, 26129 Oldenburg, Germany;

Email: stephan.heise@dlr.de

Authors

Kai Gehrke – German Aerospace Center (DLR), Institute of Networked Energy Systems, 26129 Oldenburg, Germany

Laura Campos Guzman – German Aerospace Center (DLR), Institute of Solar Research, 04005 Almería, Spain

Martin Vehse – German Aerospace Center (DLR), Institute of Networked Energy Systems, 26129 Oldenburg, Germany

Carsten Agert – German Aerospace Center (DLR), Institute of Networked Energy Systems, 26129 Oldenburg, Germany

Complete contact information is available at: https://pubs.acs.org/10.1021/acsaem.5c02770

Notes

The authors declare no competing financial interest.

ACKNOWLEDGMENTS

E.S. is supported by a DLR-DAAD fellowship, with reference number 91867011. The authors would like to thank Chris Sturm from the Felix Bloch institute for solid state physics of the university of Leipzig for the ellipsometry measurements and prof. Mercedes Gabas from the solar energy institute of the technical university of Madrid for providing the data on the refractive index and absorption coefficient of germanium.

REFERENCES

- (1) Burger, T.; Sempere, C.; Roy-Layinde, B.; Lenert, A. Present Efficiencies and Future Opportunities in Thermophotovoltaics. *Joule* **2020**, *4* (8), 1660–1680.
- (2) LaPotin, A.; Schulte, K. L.; Steiner, M. A.; Buznitsky, K.; Kelsall, C. C.; Friedman, D. J.; Tervo, E. J.; France, R. M.; Young, M. R.; Rohskopf, A.; Verma, S.; Wang, E. N.; Henry, A. Thermophotovoltaic efficiency of 40. *Nature* **2022**, *604* (7905), 287–291.
- (3) Zhou, Z.; Sakr, E.; Sun, Y.; Bermel, P. Solar thermophotovoltaics: reshaping the solar spectrum. *Nanophotonics* **2016**, *S* (1), 1–21.
- (4) Li, H.; Wan, S.; Wang, L.; Zhao, J.; Ji, D. Divide and conquer: Spectral-splitting and utilization of thermal radiation from waste heat in the steel industry. *Appl. Energy* **2025**, *378*, No. 124836.
- (5) Datas, A.; Martí, A. Thermophotovoltaic energy in space applications: Review and future potential. *Sol. Energy Mater. Sol. Cells* **2017**, *161*, 285–296.
- (6) Nelson, R. E. A brief history of thermophotovoltaic development. *Semicond. Sci. Technol.* **2003**, *18* (5), S141–S143.
- (7) Omair, Z.; Scranton, G.; Pazos-Outón, L. M.; Xiao, T. P.; Steiner, M. A.; Ganapati, V.; Peterson, P. F.; Holzrichter, J.; Atwater, H.; Yablonovitch, E. Ultraefficient thermophotovoltaic power conversion by band-edge spectral filtering. *Proc. Natl. Acad. Sci. U.S.A.* 2019, 116 (31), 15356–15361.
- (8) Fan, D.; Burger, T.; McSherry, S.; Lee, B.; Lenert, A.; Forrest, S. R. Near-perfect photon utilization in an air-bridge thermophotovoltaic cell. *Nature* **2020**, *586* (7828), 237–241.
- (9) Roy-Layinde, B.; Lim, J.; Arneson, C.; Forrest, S. R.; Lenert, A. High-efficiency air-bridge thermophotovoltaic cells. *Joule* **2024**, *8* (7), 2135–2145.
- (10) Gamel, M.; López, G.; Medrano, A. M.; Jiménez, A.; Datas, A.; Garín, M.; Martín, I. Highly reflective and passivated ohmic contacts in p-Ge by laser processing of aSiCx:H(i)/Al2O3/aSiC films for thermophotovoltaic applications. *Sol. Energy Mater. Sol. Cells* **2024**, 265, No. 112622.
- (11) Fernández, J.; Dimroth, F.; Oliva, E.; Hermle, M.; Bett, A. W. In *Back-Surface Optimization of Germanium TPV Cells*, AIP Conference Proceedings; AIP, 2007; pp 190–197.
- (12) van der Heide, J.; Posthuma, N. E.; Flamand, G.; Geens, W.; Poortmans, J. Cost-efficient thermophotovoltaic cells based on germanium substrates. *Sol. Energy Mater. Sol. Cells* **2009**, 93 (10), 1810–1816.

- (13) Martín, P.; Orejuela, V.; Sanchez-Perez, C.; García, I.; Rey-Stolle, I. In *Device Architectures for Germanium TPV Cells with Efficiencies over 30%*, 2023 14th Spanish Conference on Electron Devices (CDE); IEEE, 2023; pp 1–4.
- (14) Martín, P.; Orejuela, V.; Cano, A.; García, I.; Luque, A.; Rey-Stolle, I. Cost-effective 23.2% efficient germanium thermophotovoltaic converters for thermal batteries. *Cell Rep. Phys. Sci.* **2024**, 5 (10), No. 102231.
- (15) Martín, I.; López, G.; Garín, M.; Ros, E.; Ortega, P.; Voz, C.; Puigdollers, J. Hole selective contacts based on transition metal oxides for c-Ge thermophotovoltaic devices. *Sol. Energy Mater. Sol. Cells* **2023**, *251*, No. 112156.
- (16) Cao, S.; Li, J.; Zhang, J.; Lin, Y.; Lu, L.; Wang, J.; Yin, M.; Yang, L.; Chen, X.; Li, D. Stable MoO X -Based Heterocontacts for p -Type Crystalline Silicon Solar Cells Achieving 20% Efficiency. *Adv. Funct. Mater.* **2020**, 30 (49), No. 2004367, DOI: 10.1002/adfm.202004367.
- (17) Koida, T.; Fujiwara, H.; Kondo, M. Hydrogen-doped In 2 O 3 as High-mobility Transparent Conductive Oxide. *Jpn. J. Appl. Phys.* **2007**, *46* (7L), No. L685.
- (18) Schultes, M.; Helder, T.; Ahlswede, E.; Aygüler, M. F.; Jackson, P.; Paetel, S.; Schwenzer, J. A.; Hossain, I. M.; Paetzold, U. W.; Powalla, M. Sputtered Transparent Electrodes (IO:H and IZO) with Low Parasitic Near-Infrared Absorption for Perovskite—Cu(In,Ga)Se 2 Tandem Solar Cells. ACS Appl. Energy Mater. 2019, 2 (11), 7823—7831.
- (19) Erfurt, D.; Heinemann, M. D.; Körner, S.; Szyszka, B.; Klenk, R.; Schlatmann, R. Improved electrical properties of pulsed DC magnetron sputtered hydrogen doped indium oxide after annealing in air. *Mater. Sci. Semicond. Process.* **2019**, *89*, 170–175.
- (20) Theiss, M. Hard and Software for Optical Spectroscopy, Dr. Bernhard-Klein-Str. 110, 52078 Aachen, Germany. 2013.
- (21) Scherg-Kurmes, H.; Seeger, S.; Körner, S.; Rech, B.; Schlatmann, R.; Szyszka, B. Optimization of the post-deposition annealing process of high-mobility In2O3:H for photovoltaic applications. *Thin Solid Films* **2016**, *599*, 78–83.
- (22) Calnan, S.; Tiwari, A. N. High mobility transparent conducting oxides for thin film solar cells. *Thin Solid Films* **2010**, *518* (7), 1839–1849.
- (23) Gessert, T. A.; Burst, J.; Li, X.; Scott, M.; Coutts, T. J. Advantages of transparent conducting oxide thin films with controlled permittivity for thin film photovoltaic solar cells. *Thin Solid Films* **2011**, *519* (21), 7146–7148.
- (24) Cui, C.; Ding, Q.; Yu, S.; Yu, C.; Jiang, D.; Hu, C.; Gu, Z.; Zhu, J. Strategies to break the trade-off between infrared transparency and conductivity. *Prog. Mater. Sci.* **2023**, *136*, No. 101112.
- (25) Holman, Z. C.; Filipič, M.; Descoeudres, A.; De Wolf, S.; Smole, F.; Topič, M.; Ballif, C. Infrared light management in high-efficiency silicon heterojunction and rear-passivated solar cells. *J. Appl. Phys.* **2013**, *113* (1), No. 013107, DOI: 10.1063/1.4772975.
- (26) Würfel, P. The Chemical Potential of Radiation. *J. Phys. C: Solid State Phys.* **1982**, *15*, 3967–3985.
- (27) Omair, Z.; Menon, V.; Oduor, P.; Choi, K.-K.; Dutta, A. K. In *Ultra-Broadband Omnidirectional-Distributed Bragg-Reflectors for Near-IR to Longwave-IR Thermophotovoltaic Devices*, Energy Harvesting and Storage: Materials, Devices, and Applications XII; Balaya, P.; Das, N. C.; Xu, S., Eds.; SPIE, 2022; p 15.
- (28) Blanco, E.; Martín, P.; Domínguez, M.; Fernández-Palacios, P.; Lombardero, I.; Sanchez-Perez, C.; García, I.; Algora, C.; Gabás, M. Refractive indices and extinction coefficients of p-type doped Germanium wafers for photovoltaic and thermophotovoltaic devices. *Sol. Energy Mater. Sol. Cells* **2024**, *264*, No. 112612.
- (29) Scherg-Kurmes, H.; Körner, S.; Ring, S.; Klaus, M.; Korte, L.; Ruske, F.; Schlatmann, R.; Rech, B.; Szyszka, B. High mobility In2O3:H as contact layer for a-Si:H/c-Si heterojunction and μ c-Si:H thin film solar cells. *Thin Solid Films* **2015**, *594*, 316–322.
- (30) Erfurt, D.; Heinemann, M. D.; Schmidt, S. S.; Körner, S.; Szyszka, B.; Klenk, R.; Schlatmann, R. Influence of ZnO-Based Sub-Layers on the Growth of Hydrogen Doped Indium Oxide. *ACS Appl. Energy Mater.* **2018**, *1* (10), 5490–5499.

(31) Sun, X.; Yang, Z.; Hwang, H.-L. Short-circuit current density and fill factor improvement by optimizing In2O3:H and metal back reflector layers for p-i-n a-SiGe:H thin film solar cells. *J. Mater. Sci.: Mater. Electron.* **2019**, 30 (19), 17759–17764.



ı

CAS BIOFINDER DISCOVERY PLATFORM™

BRIDGE BIOLOGY AND CHEMISTRY FOR FASTER ANSWERS

Analyze target relationships, compound effects, and disease pathways

Explore the platform

